Hydrogen Storage Properties of a New Ti-V-Cr-Zr-Nb High Entropy Alloy

Anis Bouzidi, Laetitia Laversenne, V. Nassif, Erik Elkaim, Claudia Zlotea

hydrogen

MDPI

Article

Hydrogen Storage Properties of a New Ti-V-Cr-Zr-Nb High Entropy Alloy

Anis Bouzidi [1], Laetitia Laversenne [2], Vivian Nassif [2], Erik Elkaim [3] and Claudia Zlotea [1,*]

[1] University Paris Est Créteil, CNRS, ICMPE, UMR 7182, 2 rue Henri Dunant, 94320 Thiais, France; anis.bouzidi@cnrs.fr
[2] University Grenoble Alpes, CNRS, Institut Néel, 38000 Grenoble, France; laetitia.laversenne@neel.cnrs.fr (L.L.); vivian.nassif@neel.cnrs.fr (V.N.)
[3] Synchrotron SOLEIL, L'Orme des Merisiers, Saint-Aubin, BP48, 91192 Gif sur Yvette, France; erik.elkaim@synchrotron-soleil.fr
* Correspondence: claudia.zlotea@cnrs.fr

Abstract: We are reporting the synthesis, the physicochemical, and the hydrogen sorption properties of a novel *bcc* high entropy alloy $Ti_{0.30}V_{0.25}Cr_{0.10}Zr_{0.10}Nb_{0.25}$. At room temperature, the alloy rapidly absorbs hydrogen reaching a capacity of 2.0 H/M (3.0 wt.%) and forming a dihydride with *fcc* structure, as confirmed by both synchrotron X-ray diffraction and neutron diffraction. The absorption Pressure–Composition Isotherms corroborated with synchrotron X-ray diffraction prove that the reaction with hydrogen occurs within two steps, i.e., *bcc* alloy → *bcc* monohydride → *fcc* dihydride. The thermodynamic parameters calculated for the second step transformation evidence the formation of a stable dihydride with $\Delta H_{abs} = -75$ kJ/molH_2. The phase transition during hydrogen/deuterium desorption was investigated by in situ synchrotron X-ray and neutron diffraction confirming a reversible reaction with hydrogen. Furthermore, the cycling properties show a decrease of the capacity over the first cycles followed by a stabilization at 2.44 wt.%, whereas the absorption kinetics improve after the first cycle reaching full capacity after only 30 s at room temperature.

Keywords: high entropy alloy; hydrogen storage; synchrotron X-ray diffraction; neutron diffraction; thermodynamic properties

Citation: Bouzidi, A.; Laversenne, L.; Nassif, V.; Elkaim, E.; Zlotea, C. Hydrogen Storage Properties of a New Ti-V-Cr-Zr-Nb High Entropy Alloy. *Hydrogen* **2022**, *3*, 270–284. https://doi.org/10.3390/hydrogen3020016

Academic Editor: Thomas Klassen

Received: 11 May 2022
Accepted: 2 June 2022
Published: 16 June 2022

1. Introduction

To ensure the reduction of carbon emissions and the transition towards a clean, sustainable, and safe energy system hydrogen has the potential to fulfil all requirements as a future energy carrier due to its abundance and its large chemical energy per mass when compared to other chemical fuels [1]. As an energy carrier, hydrogen needs to be produced, transported, stored, and, finally, used in practical applications. Among all steps, hydrogen storage is considered a bottleneck for further development of hydrogen-based economy. Hydrogen can be stored in three different ways: as compressed gas at high pressure, as cryogenic liquid at very low temperature, and in solid-state materials. The latter method is the safest and most efficient form to increase the volumetric hydrogen density [2]. A large range of materials have been studied for hydrogen storage, such as complex and salt-like hydrides [3], alloys, and intermetallics [4–6] but none of these fulfilled the requirements for the use in practical devices.

A new class of materials called high entropy alloys (HEA), initially proposed in 2004 for enhancing mechanical properties [7,8], started to attract widespread research interest due to their interesting hydrogen storage performances [9]. HEAs are defined as alloys containing at least five principal elements with a composition range between 5 and 35 at.% for each element. The HEAs are random solid solutions adopting simple crystalline structures such as, body centered cubic (*bcc*), face centered cubic (*fcc*), and hexagonal close-packed (*hcp*) lattices. The formation of *bcc* or *fcc* solid solutions in HEAs can be predicted following

two empirical parameters: the atomic size difference (δ) as defined previously [10] and the valence electron concentration (VEC) [11]. Empirically, it has been established that HEAs stabilizing in solid solutions have δ < 6.6% [12] whereas single-phase *bcc* HEAs possess a VEC < 6 [13].

In 2016, Sahlberg et al., reported the *bcc* TiVZrNbHf alloy that reaches a high capacity of absorption of 2.5 H/M, overpassing the maximum uptake known for conventional alloys and metals [14]. Since then, several HEAs with *bcc* lattice have been reported with interesting hydrogen storage performances [15,16]. However, obtaining *bcc* alloys is not the merely criterion for reaching high capacities of hydrogen storage but the chemical composition of the HEAs also plays an important role.

In order to understand the effect of the composition on the hydrogen storage properties, our group has developed an original strategy based on the investigation of the effect of the addition of 10 at.% of a new element in an initial quaternary Ti-V-Zr-Nb alloy on the hydrogen sorption properties. Firstly, Montero et al. optimized the synthesis of the pristine quaternary composition $Ti_{0.325}V_{0.275}Zr_{0.125}Nb_{0.275}$ to obtain a *bcc* single-phase alloy using different synthetic methods (arc melting, ball milling) [17]. This quaternary alloy undergoes a phase transition from the initial *bcc* alloy to a *fcc* hydride phase with a capacity of 1.7 H/M (2.5 wt.%). Subsequently, our strategy entails the addition of 10 at.% of a fifth element to the optimized $Ti_{0.325}V_{0.275}Zr_{0.125}Nb_{0.275}$ composition, such as Ta [18], Al [19], Mg [20], and Mo [21]. All novel $Ti_{0.30}V_{0.25}Zr_{0.10}Nb_{0.25}M_{0.10}$ compositions (*M* = Ta, Al, Mg, and Mo) crystallize into a single-phase *bcc* lattice and reach high gravimetric capacities, such as 2.5, 2.6, 2.7, and 2.8 wt.% for Ta, Al, Mg, and Mo containing alloys, respectively. Other properties can be also positively affected by the presence of a fifth element, such as the desorption temperature which strongly reduces in the case of alloys with 10 at.% Al and Ta and the cycling stability which increases in the presence of 10 at.% Al and Mg. This strategy confirms that the addition of a fifth element to the quaternary composition can upgrade the storage capacity and can help rationalize the effect of the chemical composition on the hydrogen storage performances of refractory HEAs.

Along with the previous examples, Cr addition in refractory HEAs also seems a promising approach to tailor the hydrogen absorption properties. Strozi et al. studied the effect of the Cr addition in the ternary equimolar TiVNb by adding the following concentrations: 15, 25, and 35 at.% Cr [22]. The gravimetric capacities depend upon the composition and reach almost 3.0, 2.7, and 2.8 wt.% for $(TiVNb)_{85}Cr_{15}$, $(TiVNb)_{75}Cr_{25}$, and $(TiVNb)_{65}Cr_{35}$, respectively. The amount of the added Cr affects not only the absorption capacity, but also the Pressure Composition Isotherm (PCI) at room temperature. The $(TiVNb)_{85}Cr_{15}$ alloy shows an unique plateau-like PCI at rather low equilibrium values, whereas for the other compositions the PCIs shows two plateaus at higher pressures indicating a two-phase transition [22]. Thus, Cr concentration can effectively tune the capacity and the equilibrium pressure at room temperature. Very recently, Park et al. studied the hydrogen absorption properties of the equimolar TiZrVNbCr alloy [23]. This composition is multiphased with a mixture of *bcc* and *fcc* lattices and a modest hydrogen absorption capacity of 1.77 wt.% [23].

In this context and following our aforementioned strategy, we report presently on the effect of 10 at.% Cr addition into the quaternary $Ti_{0.325}V_{0.275}Zr_{0.125}Nb_{0.275}$ alloy. A novel $Ti_{0.30}V_{0.25}Cr_{0.10}Zr_{0.10}Nb_{0.25}$ high entropy alloy was prepared and thoroughly characterized by a large palette of experimental techniques from laboratory to large-scale facilities. The effect of Cr addition into the physicochemical and the hydrogen absorption properties of the pristine alloy is highlighted and compared to previous results.

2. Materials and Methods

The alloy $Ti_{0.30}V_{0.25}Cr_{0.10}Zr_{0.10}Nb_{0.25}$ was prepared starting from high purity elements Ti (99.99%), V (99.7%), Zr (99.95%), Nb (99.95%), and Cr (99.99%) by high temperature arc melting under argon atmosphere to avoid any contaminations.

Ex situ structural characterizations were carried out using the laboratory X-ray powder diffractometer D8 advance Bruker (Cu Kα radiation, Bragg–Brentano geometry) and the SOLEIL synchrotron radiation (SR-XRD) at the Cristal beamline (λ = 0.7289 Å). For the ex situ SR-XRD, the powder samples were charged in a capillary tube of 0.2 mm diameter. The scanning range was from 1° to 85° (2θ) within a 10-min acquisition time.

In situ SR-XRD measurements during hydrogen desorption from the hydride phase were carried out at the Cristal beamline in SOLEIL synchrotron (λ = 0.67156 Å). The sample was finely ground, mixed with fumed silica powder to reduce the X-ray absorbance, and, finally, placed in a capillary tube of 0.2 mm diameter. The SR-XRD patterns were recorded during hydrogen desorption by applying a constant temperature ramp from 25 to 450 °C (5 °C/min) under secondary vacuum. The scanning range was from 0.2° to 65° (2 θ) within a 3-min acquisition time.

In situ and ex situ powder neutron diffraction (nD) experiments on a deuterated sample were measured on the D1B beamline (λ = 1.2858 Å) at the Institute Laue–Langevin with a scanning range from 1° to 128° (2 θ°) https://doi.ill.fr/10.5291/ILL-DATA.CRG-2768. The ex situ measurements were performed at room temperature using a vanadium container while the in situ experiments were performed with a silica tube sample holder. The silica tube was connected to a secondary vacuum and the desorption was carried out by applying a constant heating rate with 1 °C/min up to 450 °C while the pressure of evolved gases was simultaneously recorded by the help of a vacuum gauge.

The collected powder diffraction data were refined using the Rietveld method with Fullprof software [24]. The peak shape was described by Thompson–Cox–Hastings Pseudo-Voigt function.

The microstructure analysis was performed by Scanning Electron Microscopy (SEM) acquiring back-scattered electron signal (BSE) using a Zeiss Merlin microscope. The as-cast and after cycling samples were embedded in a resin and coated with 1.9 nm of Pd. The chemical mapping of the sample was performed by energy dispersive X-ray spectroscopy (EDS).

Hydrogen absorption properties were determined by measuring the Pressure–Composition Isotherms (PCI) at several temperatures. The PCI curves were recorded using a homemade volumetric device with thermostatically calibrated volumes at 25 °C. Small pieces of the sample were placed inside a stainless-steel sample holder and firstly activated by a heat treatment at 350 °C under dynamic vacuum for 3 h. For the calculation of the hydrogen uptake, the real equation of state for hydrogen was used from the program GASPAK V3.32 (Cryodata. Inc., Boulder, CO, USA). The Van't Hoff equation (Equation (1)) was employed to evaluate the enthalpy and the entropy from the measured PCIs [25].

$$\ln\left(\frac{P_{eq}}{p^0}\right) = \frac{\Delta H}{RT} - \frac{\Delta S}{R} \quad (1)$$

The cycling measurements (absorption/desorption) were performed using the same volumetric device. The absorption was performed at 50 bar H_2 pressure at 25 °C during which the absorption kinetic curve was recorded, while the desorption was carried out by heating at 450 °C under dynamic vacuum for 3 h.

3. Results and Discussions

The VEC and the lattice distortion parameter (δ) of the studied composition $Ti_{0.30}V_{0.25}Cr_{0.10}Zr_{0.10}Nb_{0.25}$ are 4.7 and 6.69%, respectively (the radius of each element is taken from reference [26]). Cr is the element with the smallest radius and relatively far from the rest of the components, r_{Cr} = 1.25 Å < r_V = 1.31 Å < r_{Nb} = 1.43 Å < r_{Ti} = 1.45 Å < r_{Zr} = 1.59 Å, which increases the atom size disparity in the alloy. Consequently, the lattice distortion parameter δ = 6.69% is larger than the value for the pristine quaternary alloy δ = 6.0 % (without Cr) [17]. Moreover, Cr addition into the original quaternary alloy increases the VEC parameter from 4.55 to 4.7 [17].

Concerning the empirical predictions of the phase stability, the δ parameter for the present alloy is at the limit for obtaining solid solutions (6.6 %) [12] and the VEC is in the range of alloys adopting *bcc* lattice (VEC < 6) [13]. Indeed, the as-cast alloy crystallizes in a *bcc* lattice (see XRD pattern in Figure 1) with the parameter a_{bcc} = 3.225 (1) Å, as determined by Rietveld refinement. However, the alloy is not single-phased, since the presence of an unknown small impurity at 2 θ~34.5° can be noticed in the XRD pattern (marked with * Figure 1).

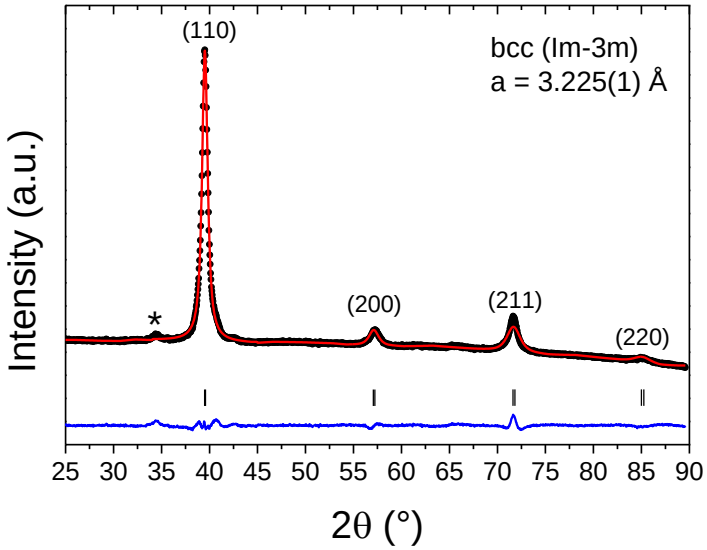

Figure 1. X-ray diffraction pattern (λ = 1.5406 Å) of the as-cast $Ti_{0.30}V_{0.25}Cr_{0.10}Zr_{0.10}Nb_{0.25}$ with the corresponding Rietveld analysis; star symbol indicates a small impurity. The asterisk is indicating the presence of a small unknown impurity.

Compared to the pristine quaternary alloy, the lattice parameter decreases from a_{bcc} = 3.261 (1) Å [17] to a_{bcc} = 3.225 (1) Å by Cr addition. This can be explained by the fact that Cr has the smallest atomic radius among all constituents into the quinary alloy, as discussed above. This increases the δ and reduces the *bcc* lattice parameter, relative to the pristine quaternary composition.

The microstructure and chemical homogeneity of the alloy was investigated by SEM-EDS (Figure 2).

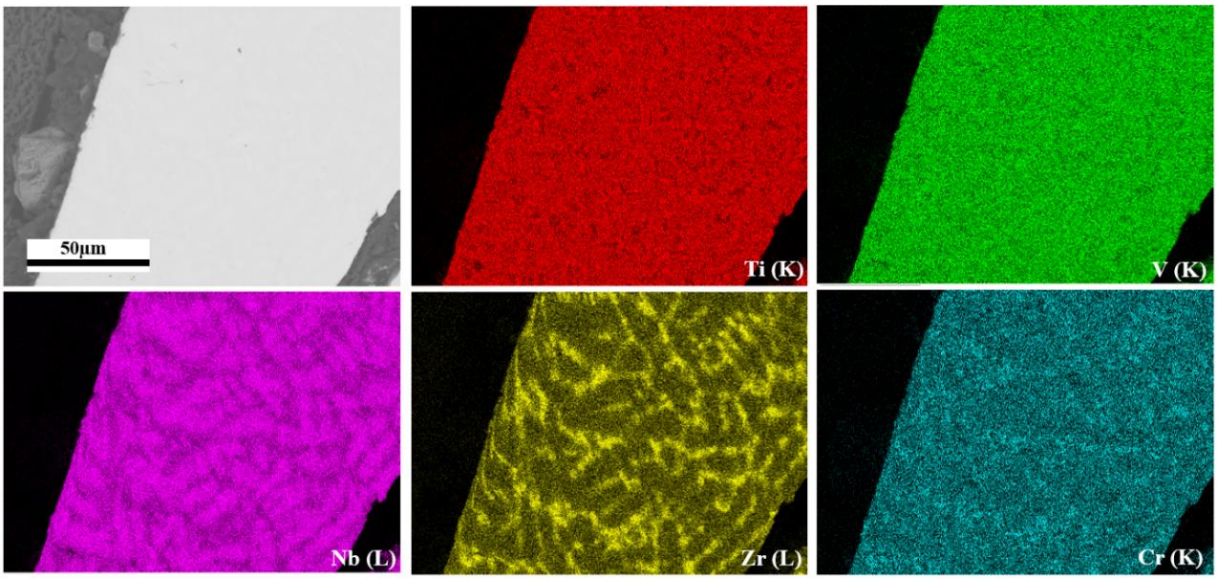

Figure 2. SEM image and related EDS chemical mapping of the as-cast $Ti_{0.30}V_{0.25}Cr_{0.10}Zr_{0.10}Nb_{0.25}$ alloy.

The SEM-EDS analysis shows the presence of dendritic and interdendritic regions similar to previous observations reported for refractory HEAs, such as, TiZrNbHfTa [27] or $Ti_{0.30}V_{0.25}Zr_{0.10}Nb_{0.25}Mo_{0.10}$ HEA [21]. However, the overall chemical composition is close to the nominal one (Table 1). From the chemical analyses in Table 1, Nb and Zr elements have the largest deviation from the nominal composition. The dendrites are rich in Nb and poor in Zr and Cr, whereas the interdendritic region is rich in Zr and Cr as well as poor in Nb relative to the nominal concentration. The Ti and V values are close to the nominal composition, irrespective of the region. This composition modulation between the dendrites and the interdendritic regions can be accounted by the distribution of the alloying elements in the liquid and the solid phases during solidification. A Nb-rich solid phase (dendrite) is firstly formed during solidification because of the higher melting temperature of Nb compared to the four other elements.

Table 1. EDS chemical analysis of the different regions in the as-cast alloy and the overall composition.

Region	Ti (at.%)	V (at.%)	Cr (at.%)	Zr (at.%)	Nb (at.%)
Dendritic	30.2 (0.5)	25.1 (0.4)	8.1 (0.4)	5.8 (0.5)	30.8 (1.2)
Interdendritic	29.9 (1.1)	23.4 (0.7)	11.1 (0.8)	18.5 (1.5)	17.1 (1.8)
Overall	30.5 (0.1)	25.4 (0.6)	9.5 (0.5)	10.3 (0.6)	24.3 (1.1)
Nominal	30	25	10	10	25

After the synthesis of a homogeneous *bcc* $Ti_{0.30}V_{0.25}Cr_{0.10}Zr_{0.10}Nb_{0.25}$ alloy, the next step is the investigation of the hydrogen absorption/desorption properties. Figure 3 shows the PCIs recorded in the temperature range from 25 to 300 °C. At room temperature, the $Ti_{0.30}V_{0.25}Cr_{0.10}Zr_{0.10}Nb_{0.25}$ alloy can absorb up to maximum 2.0 H/M i.e., 3.0 wt.%. Thus, the 10 at.% Cr addition into the pristine quaternary alloy positively impacts the storage capacity which enhances from 1.7 H/M (2.5 wt.%) in the pristine materials [17] to 2.0 H/M (3.0 wt.%) in the present composition. Furthermore, it might be interesting to compare this capacity to alloys from the same family $Ti_{0.30}V_{0.25}Zr_{0.10}Nb_{0.25}M_{0.10}$ (M = Al, Mo, Mg and Ta) already reported, see Table 2. The present material has the highest gravimetric capacity, whereas the capacities of the other alloys are inferior ranging from 2.5 to 2.8 wt.%. Moreover, the gravimetric capacities of other well-known intermetallics, such as TiFe (1.89 wt.%) [28] and $LaNi_5$ (1.4 wt.%) [28], are also smaller, compared to the present alloy.

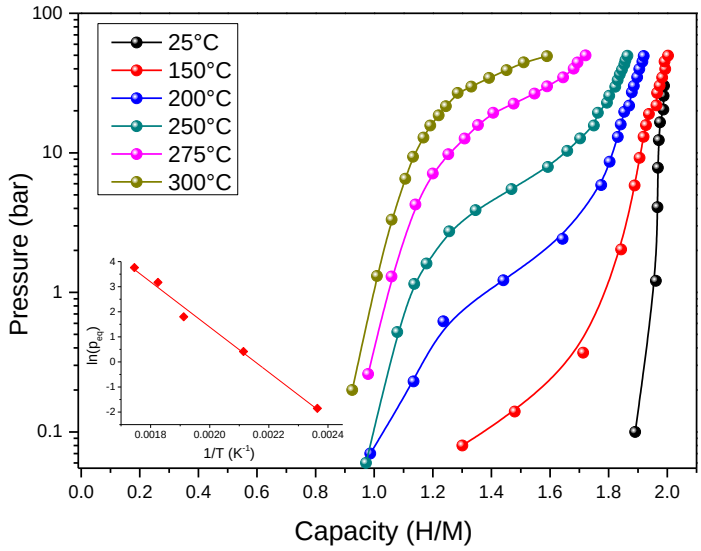

Figure 3. Pressure Composition Isotherms of the $Ti_{0.30}V_{0.25}Cr_{0.10}Zr_{0.10}Nb_{0.25}$ alloy at various temperatures from 25 °C to 300 °C. The inset shows the Van't Hoff plot ($\ln(p_{eq})$ vs. 1/T).

Table 2. Comparison of the hydrogen storage properties of similar HEAs.

Composition	As-Cast Phase	Hydride Phase	Capacity (wt.%)	Reference
$Ti_{0.30}V_{0.25}Cr_{0.10}Zr_{0.10}Nb_{0.25}$	*bcc*	*fcc*	3.0	Present study
$Ti_{0.325}V_{0.275}Zr_{0.125}Nb_{0.275}$	*bcc*	*fcc*	2.5	[17]
$Ti_{0.30}V_{0.25}Zr_{0.10}Nb_{0.25}Mo_{0.10}$	*bcc*	*fcc*	2.8	[21]
$Ti_{0.30}V_{0.25}Zr_{0.10}Nb_{0.25}Al_{0.10}$	*bcc*	*bct*	2.6	[19]
$Ti_{0.30}V_{0.25}Zr_{0.10}Nb_{0.25}Mg_{0.10}$	*bcc*	*fcc*	2.7	[20]
$Ti_{0.30}V_{0.25}Zr_{0.10}Nb_{0.25}Ta_{0.10}$	*bcc*	*fcc*	2.5	[18]

The equilibrium pressure from the PCI curve at room temperature is very low, within the limit of the pressure gauge (10^{-2} bar). At higher temperature, the PCIs curves clearly show a two-step reaction with hydrogen: one transition occurs at a very low equilibrium pressure forming a monohydride (1 H/M) and another reaction at a higher pressure leading to a dihydride (2 H/M). The equilibrium pressure of the second event increases with temperature, which allows us to calculate the variation of the enthalpy (ΔH_{abs}) and entropy (ΔS_{abs}) of the absorption reaction using Van't Hoff equation (Equation (1)). The results are listed in Table 3 together with thermodynamic values obtained for other compositions reported previously [29,30]. These results prove that the present alloy forms a very stable dihydride phase with the lowest ΔH_{abs} value among the selected materials. Discrepancies can be noticed for the ΔS_{abs} values, which are expected to be close to the entropy of gaseous hydrogen i.e., −130 J/K mol H_2. This might be due to the slopping nature of the PCI curves, which may introduce errors in the thermodynamic evaluation [31].

Table 3. $V_{0.25}Cr_{0.10}Zr_{0.10}Nb_{0.25}$ alloy absorbs hydrogen in two steps forming a dihydride phase at maximum capacity.

Composition	ΔH_{abs} (KJ/mol H_2)	ΔS_{abs} (J/Kmol H_2)	Reference
$Ti_{0.30}V_{0.25}Cr_{0.10}Zr_{0.10}Nb_{0.25}$	−75 (±4)	−161 (±8)	Present work
$(TiVNb)_{85}Cr_{15}$	−67 (±2)	−172 (±4)	[29]
TiVZrNb	−67.6	−90.3	[30]
TiVZrNbHf	−61.8	−88	[30]
$TiV_{0.5}ZrNbHf$	−59.1	−87.4	[30]

The structural characterization of this phase was performed by SR-XRD and nD for the hydrogenated and the deuterated phases, respectively (Figure 4).

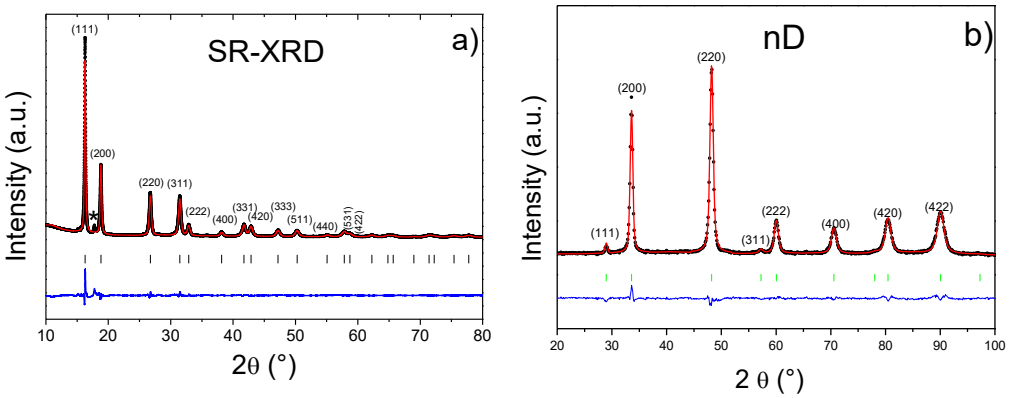

Figure 4. (**a**) SR-XRD pattern (λ = 0.7289 Å) of the dihydride $Ti_{0.30}V_{0.25}Cr_{0.10}Zr_{0.10}Nb_{0.25}H_2$, and (**b**) nD pattern (λ = 1.2858 Å) of the deuteride $Ti_{0.30}V_{0.25}Cr_{0.10}Zr_{0.10}Nb_{0.25}D_2$ and the corresponding Rietveld analyses. The star symbol indicates the presence of a minor impurity visible only by SR-XRD.

The analysis of the SR-XRD diffraction pattern of the dihydride phase in Figure 4a proves that the dihydride phase adopts a *fcc* structure (space group $Fm\bar{3}m$) with the lattice parameter a_{fcc} = 4.459 (1) Å, as determined by Rietveld analysis (see Table 4). Small impurity is also present, as marked by star, in agreement with our finding for the as-cast alloy (Figure 1). The analysis of the nD pattern in Figure 4b confirms that the deuteride crystallizes in a *fcc* type structure with a lattice parameter a_{fcc} = 4.451 (1) Å very similar to the one obtained from SR-XRD. However, the minor impurity is not visible by this method. The main advantage of neutron diffraction is the ability to locate the deuterium within the interstitial sites of the *fcc* lattice. From Rietveld refinement, the deuterium atoms occupy the tetrahedral sites of the *fcc* structure ($\frac{1}{4}$; $\frac{1}{4}$; $\frac{1}{4}$), in agreement with previous studies [18,20,21].

Table 4. Structural analysis (phase fractions and corresponding lattice parameter) of the $Ti_{0.30}V_{0.25}Cr_{0.10}Zr_{0.10}Nb_{0.25}$ alloy at different stages of the dehydrogenation process.

Hydrogen Capacity	*fcc* Dihydride Lattice Parameter (Å)	*fcc* Phase Fraction (%)	*bcc* Monohydride Lattice Parameter (Å)	*bcc* Phase Fraction (%)	*bcc* (Desorbed) Lattice Parameter (Å)	*bcc* Phase Fraction (%)
2.0 H/M	4.459(1)	100	–	–	–	–
1.3 H/M	4.399(1)	54	3.305 (1)	46	–	–
0.8 H/M	–	–	3.322 (1)	100	–	–
0.3 H/M	–	–	3.245 (5)	56	3.194 (5)	44
0.0 H/M	–	–	–	–	3.222 (2)	100

To confirm the existence of two step reaction with hydrogen, as suggested by the PCIs measurements, we used ex situ SR-XRD to characterize the alloy at different stages of the dehydrogenation process with the following capacities: three intermediate stages at 1.3 H/M, 0.8 H/M and 0.3 H/M, and the fully desorbed material at 0 H/M (Figure 5). The SR-XRD pattern of the dihydride (2.0 H/M) already presented in Figure 4a is also shown for the sake of clarity.

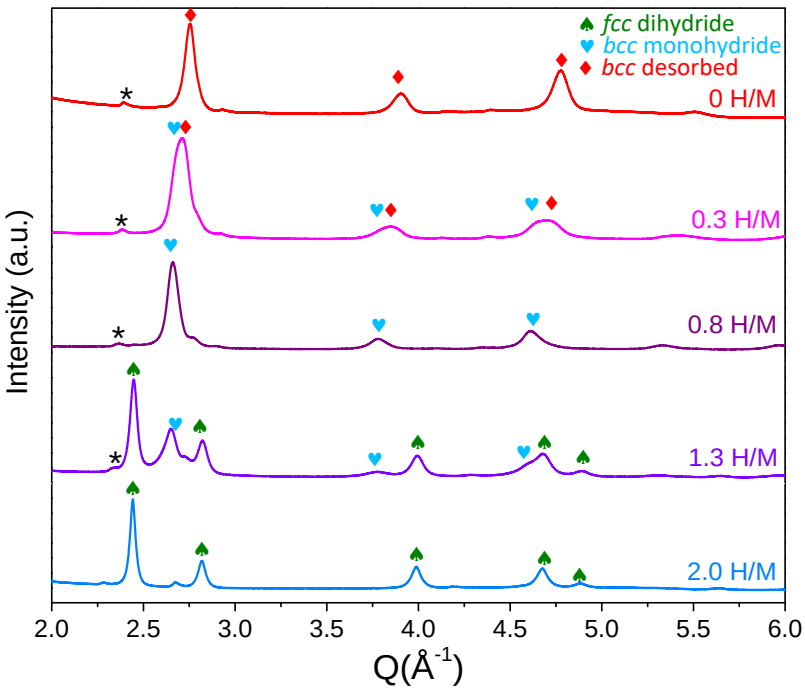

Figure 5. Ex situ SR-XRD patterns of $Ti_{0.30}V_{0.25}Cr_{0.10}Zr_{0.10}Nb_{0.25}$ at different stages of the dehydrogenation process with the following capacities: 2.0 H/M, 1.3 H/M, 0.8 H/M, 0.3 H/M, and 0 H/M. Minor impurity is marked with star symbol. The *fcc* dihydride, *bcc* monohydride and *bcc* desorbed phases are marked with green spades, blue hearts and red diamonds, respectively.

The patterns in Figure 5 were analyzed by Rietveld method (Figure SI-1 and Tables SI1–SI4) and the structural results, i.e., phase fractions and corresponding lattice parameters, are listed in Table 4.

At the intermediate capacity of 1.3 H/M, a coexistence of two phases is observed: 54% of *fcc* dihydride with 4.399 (1) Å lattice parameter and 46% of a *bcc* monohydride with lattice parameter 3.305 (1) Å. The *fcc* lattice parameter is slightly smaller relative to the value of the full dihydride 4.459 Å, probably due to slightly smaller hydrogen content compared to the fully hydrogenated material. The $Ti_{0.30}V_{0.25}Cr_{0.10}Zr_{0.10}Nb_{0.25}H_{0.8}$ (0.8 H/M) marks the formation of a single *bcc* monohydride with the lattice parameter 3.322 (1) Å. At the intermediate uptake 0.3 H/M the material contains two phases: the *bcc* monohydride is still identified (56% phase fraction) with a slightly smaller lattice parameter 3.245 (5) Å and the *bcc* desorbed phase (44% phase fraction) with lattice parameter 3.194 (5) Å, which is slightly smaller than 3.225 (1) Å of the as-cast alloy. This small discrepancy might be due to the use of different diffractometers for the characterization of the as-cast alloy (laboratory instrument) and desorbed material (synchrotron radiation). The coexistence of two phases at intermediate hydride with 0.3 H/M is also confirmed by the variation of the full width at half maximum (FWHM). The FWHM of the first peak (110) at the intermediate capacities 0.8 H/M and 0.3 H/M are 0.535° and 0.723°, respectively. The higher FWHM value for the $Ti_{0.30}V_{0.25}Cr_{0.10}Zr_{0.10}Nb_{0.25}H_{0.3}$ sample suggests the coexistence of two convoluted *bcc* phases (a *bcc* monohydride and a desorbed *bcc* phase) with very close lattice parameters. Finally, the desorbed sample adopts a *bcc* structure with a lattice parameter 3.222 (2) Å, very close to 3.225 (1) Å for the as-cast alloy, which confirms the full reversibility of the absorption/desorption reaction with hydrogen.

For an in-depth comprehension of the phase transition during desorption reaction, we have performed in situ neutron diffraction starting from the deuteride $Ti_{0.30}V_{0.25}Cr_{0.10}Zr_{0.10}Nb_{0.25}D_2$ by heating to 450 °C with 1 °C/min under dynamic vacuum (Figure 6). The desorption profile of the evolved gases during in situ nD is also plotted in the right part of Figure 6.

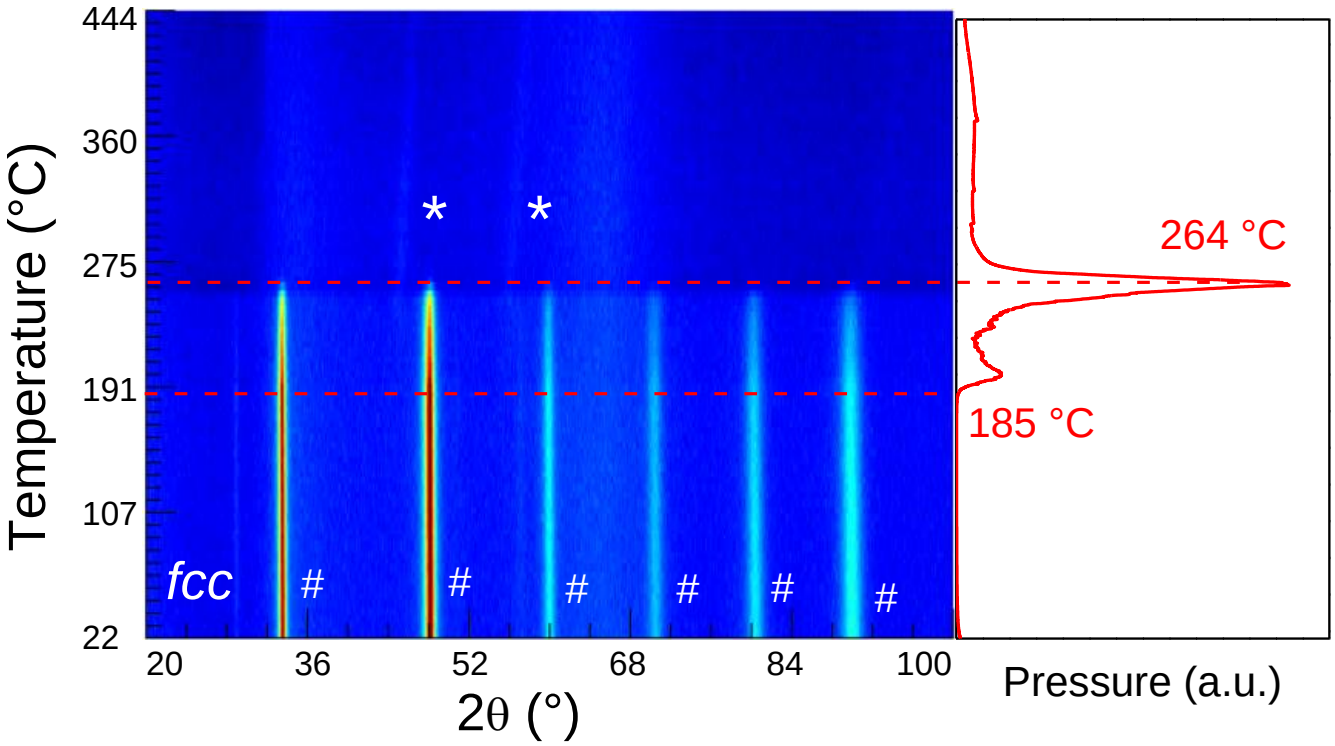

Figure 6. In situ neutron diffraction (λ = 1.2858 Å) of $Ti_{0.30}V_{0.25}Cr_{0.10}Zr_{0.10}Nb_{0.25}D_2$ during heating under dynamic vacuum from 22 °C to 445 °C with 1 °C/min (left) and the corresponding desorption profile (right). The symbol # indicates the initial *fcc* deuteride whereas, the stars indicate the desorbed phase.

Initially, there is no observable change of the diffraction peaks of the deuteride *fcc* (marked with #) up to around 185 °C, where the intensity of the diffraction peaks starts to smoothly decrease. This behavior can be accounted by the beginning of the deuterium desorption, as confirmed by the desorption profile showing a first desorption event. In the temperature range 230–265 °C, the sample experiences a sharp phase transition with the complete vanishing of the *fcc* phase due to deuterium desorption, also confirmed by the intense peak in the desorption profile at around 264 °C. After the phase transition from the deuteride to the desorbed phase, the diffraction signals are negligible, though two very weak peaks marked with * can be noticed in Figure 6. This could be explained by the very small bound coherent scattering length (b_c) of the material after deuterium desorption from 15 fm for the deuteride phase to ~2 fm for the desorbed sample. This is in agreement with many previous studies on neutron diffraction on refractory HEAs [18,20,21]. Thus, nothing can be inferred about the structure of the desorbed phase from these measurements.

It is interesting to compare these results to the in situ nD of the quaternary pristine alloy recorded under the same conditions and reported previously [19]. The alloy without Cr undergoes a sharp transition from the *fcc* dihydride to a *bcc* desorbed phase at around 270 °C without any desorption happening at lower temperature, as observed presently. This demonstrates the 10 at.% Cr addition into the initial quaternary alloy decreases the desorption temperature and consequently the stability of the *fcc* dihydride.

To better describe the structural change during desorption, we performed in situ SR-XRD measurements on $Ti_{0.30}V_{0.25}Cr_{0.10}Zr_{0.10}Nb_{0.25}H_2$ by applying a constant heating ramp from 25 to 450 °C with 5 °C/min under secondary dynamic vacuum (Figure 7a). We used Rietveld refinements to determine the phase and lattice parameter evolutions with the temperature (Figure 7b,c).

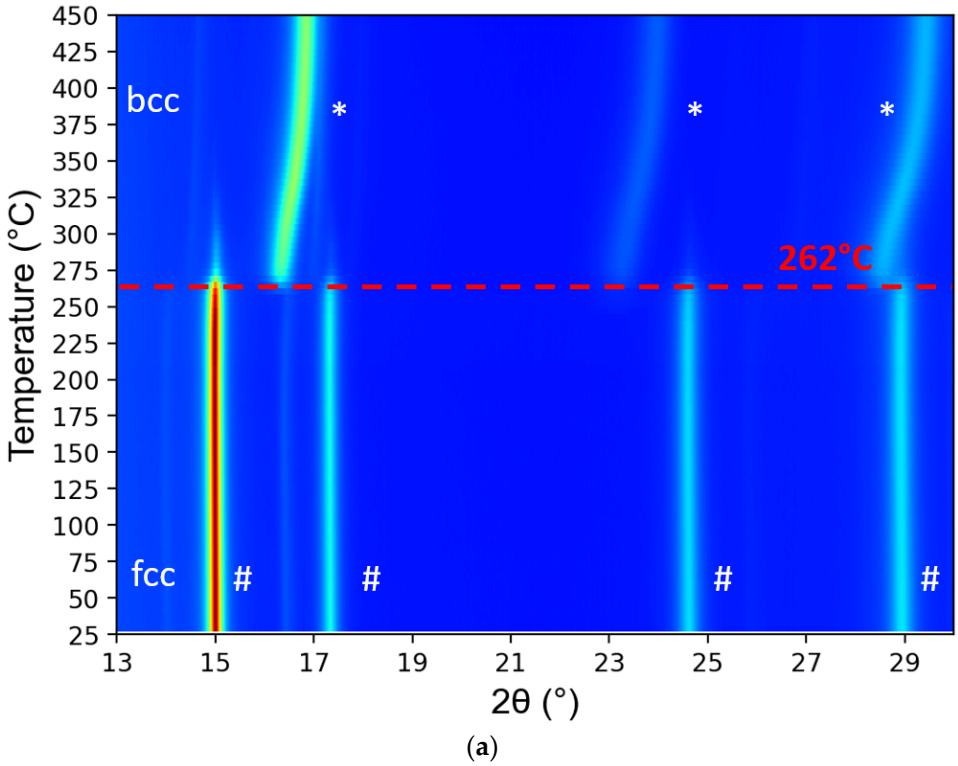

(**a**)

Figure 7. *Cont.*

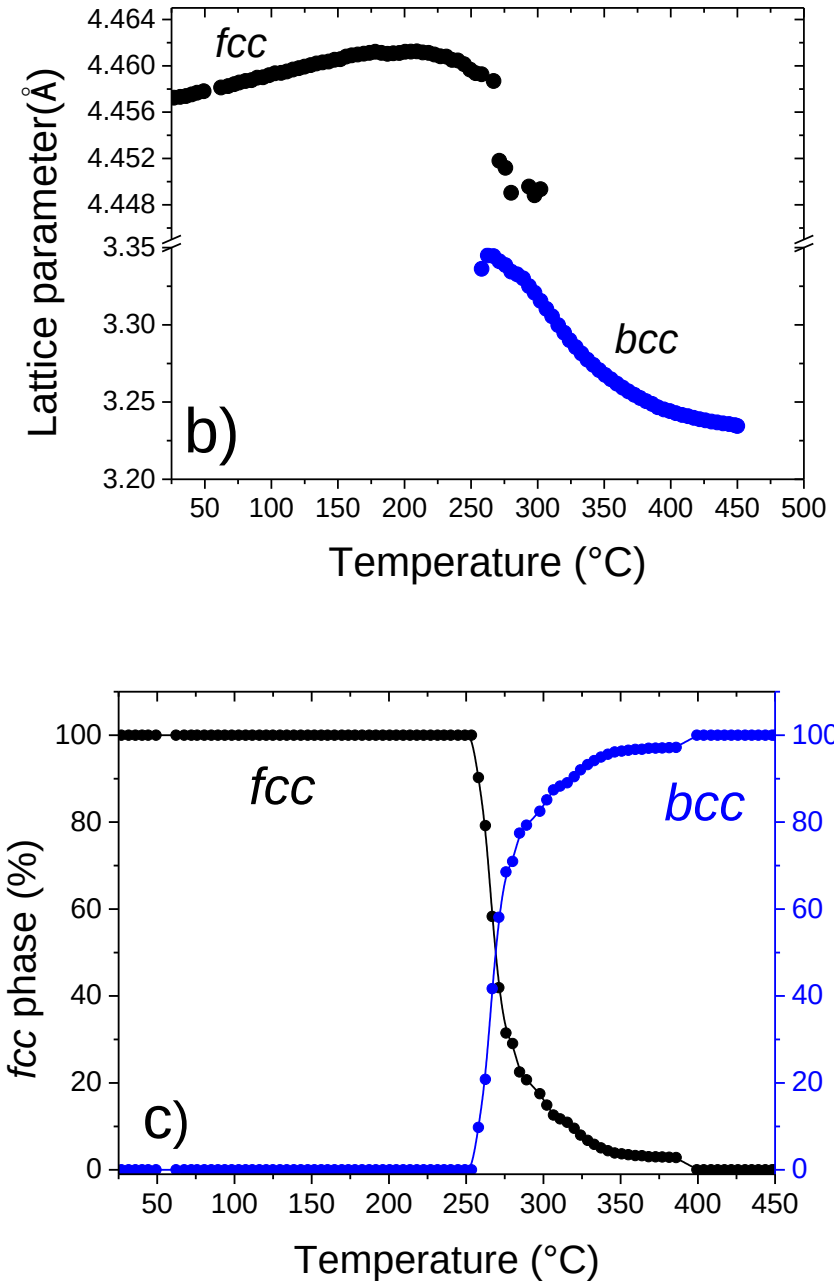

Figure 7. (**a**) In situ SR-XRD (λ = 0.67156 Å) during hydrogen desorption from $Ti_{0.30}V_{0.25}Cr_{0.10}Zr_{0.10}Nb_{0.25}H_2$ under dynamic vacuum from 25 °C to 450 °C with 5 °C/min: the initial *fcc* dihydride and the desorbed *bcc* phase are marked with # and *, respectively. (**b**) Evolution of the lattice parameter of both *fcc* and *bcc* phases during rise of the temperature.

The phase transition from the *fcc* dihydride phase to the *bcc* desorbed phase occurring at around 262 °C can be clearly noticed in Figure 7a. More structural information can be inferred from the Rietveld refinement results in Figure 7b,c. In the temperature range 25–180 °C, the *fcc* phase is stable with temperature and the lattice parameter constantly increases from 4.457 (1) Å to 4.461 (1) Å due to thermal expansion of the lattice (Figure 7b). Starting from 180 °C and up to 220 °C, the *fcc* lattice parameter stabilizes to around 4.46 Å due to concomitant thermal expansion and shrinking of the lattice by hydrogen desorption. In between 220 °C and 250 °C, the lattice parameter strongly decreases proving the major hydrogen desorption event, in agreement with nD findings. In the temperature range 250–300 °C, a phase transformation occurs with the coexistence of the *fcc* and the *bcc* phases. The *fcc* lattice parameter diminishes drastically reaching 4.449 (4) Å at around 300 °C, after

which the dihydride completely disappears. The lattice parameter of the newly formed *bcc* phase decreases smoothly with temperature from 3.336 (2) Å at 260 °C to 3.234 (2) Å at 450 °C, which can be explained by the continuous desorption of the hydrogen. The value of the *bcc* lattice parameter 3.234 (2) Å at 450 °C is slightly larger than 3.225 (1) Å obtained for the as-cast alloy due to thermal expansion.

Interestingly, the in situ SR-XRD during desorption demonstrates the existence of only one obvious phase transition from *fcc* dihydride to a *bcc* phase, whereas the PCIs during absorption and ex situ SR-XRD investigations at different stages of the dehydrogenation process put forward a two-step reaction: *fcc* dihydride → *bcc* monohydride → *bcc* desorbed phase. One possible hypothesis would be that the second transition from *bcc* monohydride to the completely desorbed *bcc* phase is not easily detected, since it implies a very small displacive rearrangement of atoms involving similar crystalline structures. Nevertheless, the in situ nD and SR-XRD results are in very good agreement, both clearly indicating a phase transition from *fcc* dihydride to *bcc* desorbed phase at similar temperatures.

The hydrogen absorption/desorption cycling in the $Ti_{0.30}V_{0.25}Cr_{0.10}Zr_{0.10}Nb_{0.25}$ HEA were performed to investigate the effect on the kinetics, the structural stability, and the reversibility of the hydrogen absorption capacity over 20 cycles (Figure 8a). The absorption reaction was performed at 25 °C under 50 bar of H_2 and the desorption was realized by heating at 450 °C for 3h under dynamic vacuum. The kinetics were recorded during the absorption step (Figure 8b). For the sake of clarity, we have also plotted the capacity variation over 20 cycles for the quaternary alloy $Ti_{0.325}V_{0.275}Zr_{0.125}Nb_{0.275}$ [17].

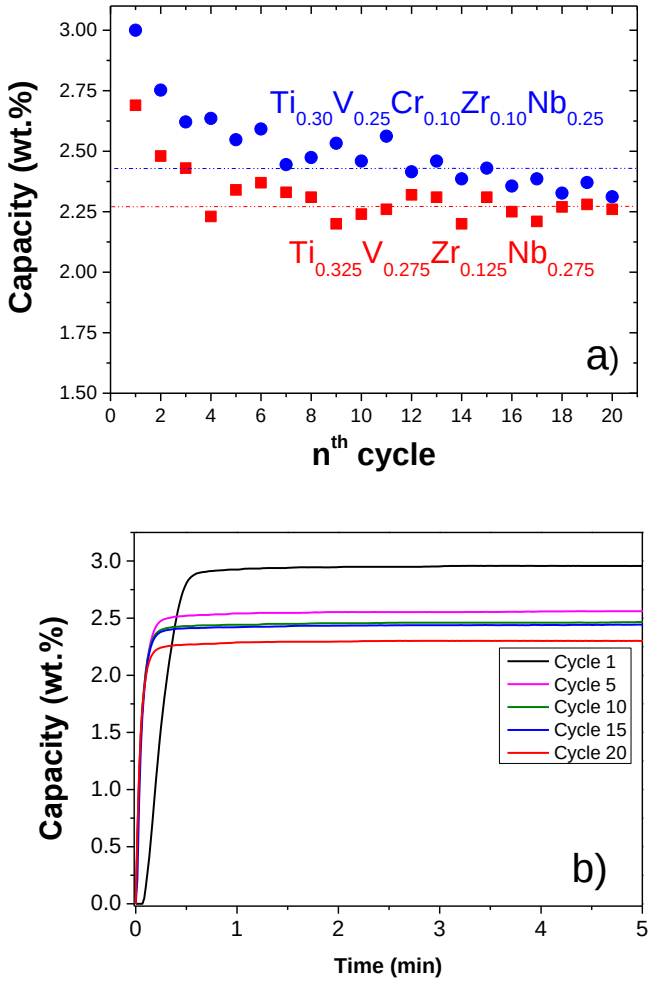

Figure 8. (**a**) Reversible hydrogen absorption capacity upon 20 absorption/desorption cycles for $Ti_{0.30}V_{0.25}Cr_{0.10}Zr_{0.10}Nb_{0.25}$ and $Ti_{0.325}V_{0.275}Zr_{0.125}Nb_{0.275}$ alloys. (**b**) Kinetic curves during absorption of hydrogen under 50 bar at 25 °C for the $Ti_{0.30}V_{0.25}Cr_{0.10}Zr_{0.10}Nb_{0.25}$ alloy.

The quinary $Ti_{0.30}V_{0.25}Cr_{0.10}Zr_{0.10}Nb_{0.25}$ alloy loses around 20% of the initial capacity (from 3.0 wt.% to 2.44 wt.%) in the first seven cycle followed by stabilization. Similarly, the quaternary alloy also undergoes a 16% reduction of the initial capacity in the first four cycles (from 2.70 wt.% to ~2.27 wt.%), followed by stabilization [21]. Thus, the 10 at.% Cr addition in the pristine quaternary alloy upgrades the stable reversible capacity from 2.27 wt.% to 2.44 wt.%. Moreover, the reversible capacity of the quinary alloy is higher than that of similar *bcc* alloys like Ti-V-Cr (1.8 wt.%) and intermetallics such as $LaNi_5$ (1.7 wt.%) and TiFe (1.89 wt.%) [32].

Many factors may lead to the loss of the capacity during hydrogen absorption/desorption cycling, for instance, the surface contamination with oxides or adsorbed hydrocarbons that are introduced from gas/vacuum contaminants or the kinetic issues that may lead to incomplete absorption or desorption or the decrease in the degree of crystallinity of the alloy. In our case, the XRD after 20 cycles of the hydride phase (Figure SI-2) proves that the *bcc* desorbed phase is still present along with the expected *fcc* hydride. This demonstrates that the absorption is not complete in our conditions, which can account for the progressive loss of the capacity during cycling.

The absorption kinetics shows a short incubation time on the first cycle (~5 s) and 90% of the full capacity is reached within 30 s. In the following cycles, all the kinetics are faster without incubation time reaching 95% of the full capacity within only 15 s (Figure 8b). The kinetics of absorption are increasing after the first cycles, probably due to the hydrogen decrepitation of the material and the creation of new clean surfaces that interact and dissociates more easily hydrogen molecules and increases the diffusion rates into the material.

The effect of the cycling on the microstructure and the chemical homogeneity of the HEA after 20 absorption/desorption cycles was studied by SEM-EDS (Figure 9). The BSE image in Figure 9 clearly shows the effect of hydrogen embrittlement with the formation of multiple cracks in the sample's grains. However, the EDS chemical mapping proves similar homogeneity as the as-cast sample with the presence of dendritic/interdendritic regions with same variation of the elements: dendritic regions are rich in Nb and poor in Zr and the interdendritic regions are rich in Zr and poor in Nb whereas, the overall composition is close to the nominal one (Ti = 30.5 at.% (±0.1); V = 25.4 at.% (±0.6); Nb = 24.3 at.% (±1.1); Zr = 10.3 at.% (±0.6); Cr = 9.5 at.% (±0.5)).

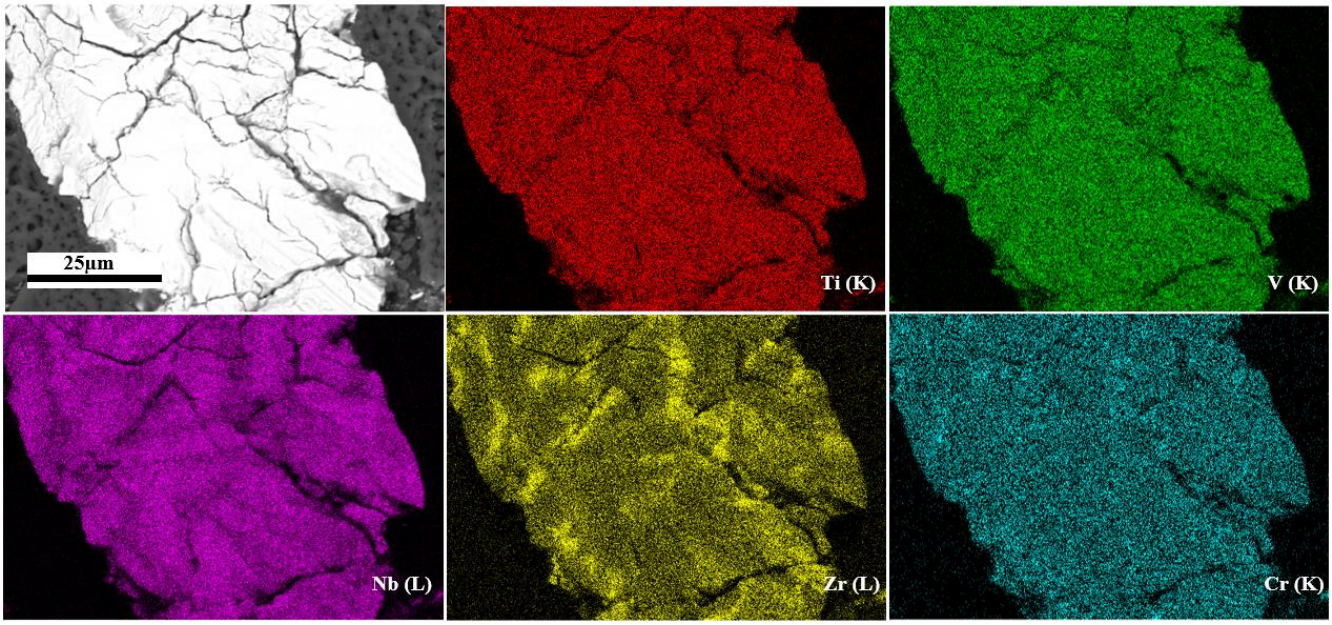

Figure 9. EDS chemical mapping and scanning electron microscopy image of the $Ti_{0.30}V_{0.25}Cr_{0.10}Zr_{0.10}Nb_{0.25}$ alloy after 20 hydrogen absorption/desorption cycles.

This demonstrates that cycling does not affect the elemental chemical homogeneity of the initial HEA and does not introduce any phase segregation.

In summary, the 10 at.% addition of Cr into the quaternary $Ti_{0.325}V_{0.275}Zr_{0.125}Nb_{0.275}$ alloy enhances the cycling properties: the initial maximum capacity of hydrogen absorption in the first cycle and the reversible hydrogen uptake after stabilization are both increasing, as compared to the pristine alloy.

4. Conclusions

The $Ti_{0.30}V_{0.25}Cr_{0.10}Zr_{0.10}Nb_{0.25}$ HEA was successfully synthesized by high temperature arc melting and adopts a *bcc* lattice with minor unknown impurity. The alloy rapidly absorbs hydrogen reaching a capacity of 2.0 H/M (3.0 wt.%), during which the alloy undergoes a two-step transition: *bcc* alloy → *bcc* monohydride → *fcc* dihydride. This sequence was confirmed by synchrotron XRD. The ex situ neutron diffraction on the deuterated *fcc* phase confirmed that the deuterium atoms occupy the tetrahedral interstitial sites. In situ synchrotron XRD and neutron diffraction experiments during hydrogen/deuterium desorption are in good agreement and prove that the transition from dihydride to monohydride occurs around 262 °C.

The comparison between the quaternary $Ti_{0.325}V_{0.275}Zr_{0.125}Nb_{0.275}$ alloy with the present $Ti_{0.30}V_{0.25}Cr_{0.10}Zr_{0.10}Nb_{0.25}$ shows an increase of the capacity from 1.7 H/M (2.5 wt.%) to 2.0 H/M (3.0 wt.%) by Cr addition. Moreover, the cycling properties are upgraded after the addition of Cr in the quaternary alloy: the reversible capacity increases from 2.27 wt.% to 2.44 wt.% for the quaternary and quinary composition, respectively. After 20 absorption/desorption cycles of the $Ti_{0.30}V_{0.25}Cr_{0.10}Zr_{0.10}Nb_{0.25}$ HEA, the SEM-EDS indicated a homogeneous chemical composition without any phase segregation. Interestingly, the addition of 10 at.% of Cr decreases the onset desorption temperature, compared to the quaternary alloy.

In conclusion, the addition of 10% of Cr into the quaternary $Ti_{0.325}V_{0.275}Zr_{0.125}Nb_{0.275}$ alloy proves to be an efficient way to boost the hydrogen storage properties. These results are very promising and open to way to rationalize the effect of the chemical composition on the hydrogen sorption properties of refractory HEAs.

Supplementary Materials: The following supporting is available online at https://www.mdpi.com/article/10.3390/hydrogen3020016/s1: Figure SI-1: Structural analysis (phase fractions and corresponding lattice parameters) of the $Ti_{0.30}V_{0.25}Cr_{0.10}Zr_{0.10}Nb_{0.25}H_x$ (x = 0.3; 0.8; 1.3) and the desorbed phase from SR-XRD. Figure SI-2: X-ray diffraction pattern after 20 absorption/desorption cycles (λ = 1.5406 Å) of the hydride $Ti_{0.30}V_{0.25}Cr_{0.10}Zr_{0.10}Nb_{0.25}H_{1.53}$. Table SI-1. Crystallographic information of the SR-XRD of the desorbed $Ti_{0.30}V_{0.25}Cr_{0.10}Zr_{0.10}Nb_{0.25}$ sample. Table SI-2. Crystallographic information of the SR-XRD of the $Ti_{0.30}V_{0.25}Cr_{0.10}Zr_{0.10}Nb_{0.25}H_{0.3}$ hydride. Table SI-3. Crystallographic information of the SR-XRD of the $Ti_{0.30}V_{0.25}Cr_{0.10}Zr_{0.10}Nb_{0.25}H_{0.8}$ hydride. Table SI-4. Crystallographic information of the SR-XRD of the $Ti_{0.30}V_{0.25}Cr_{0.10}Zr_{0.10}Nb_{0.25}H_{1.3}$ hydride.

Author Contributions: Conceptualization: C.Z.; formal analysis: A.B. and C.Z.; investigation and methodology: A.B., L.L., V.N., E.E. and C.Z.; supervision and validation: C.Z.; writing original draft: A.B. and C.Z.; writing—review and editing, A.B., L.L., V.N., E.E. and C.Z. All authors have read and agreed to the published version of the manuscript.

Funding: This research was funded by ANR MASSHY project ANR-19-CE05-0029-01.

Institutional Review Board Statement: Not applicable.

Informed Consent Statement: Not applicable.

Data Availability Statement: Not applicable.

Acknowledgments: We acknowledge 2FDN for beamtime allocation on the CRG-D1B beamline. Sofien Djellit from ILL and Fabrice Couturas from ICMPE are acknowledged for help with neutron diffraction at ILL. Jorge Montero is acknowledged for the help with SR-XRD. C.Z. and A.B. would like to thank Valérie Lalanne and Loïc Perrière from ICMPE for help with arc melting. In the framework of the CNRS Я ÉCIPROCS network, this work has been accepted for synchrotron beamtime by

the Soleil scientific proposal committee (BAG proposal 20201440). CZ would like to thank Benoit Baptiste for the help and organization of BAG beamtime on CRISTAL beamline at SOLEIL. This work has been accepted for synchrotron beamtime by the Soleil scientific on the CRISTAL beamline (proposal 20210367).

Conflicts of Interest: The authors declare no conflict of interest.

References

1. Eberle, U.; Felderhoff, M.; Schuth, F. Chemical and Physical Solutions for Hydrogen Storage. *Angew. Chem.-Int. Ed.* **2009**, *48*, 6608–6630. [CrossRef]
2. Züttel, A.; Remhof, A.; Borgschulte, A.; Friedrichs, O. Hydrogen: The Future Energy Carrier. *Philos. Trans. R. Soc. Math. Phys. Eng. Sci.* **2010**, *368*, 3329–3342. [CrossRef]
3. Milanese, C.; Jensen, T.R.; Hauback, B.C.; Pistidda, C.; Dornheim, M.; Yang, H.; Lombardo, L.; Zuettel, A.; Filinchuk, Y.; Ngene, P.; et al. Complex Hydrides for Energy Storage. *Int. J. Hydrog. Energy* **2019**, *44*, 7860–7874. [CrossRef]
4. Cohen, R.L.; West, K.W.; Wernick, J.H. Degradation of LaNi5 by Temperature-Induced Cycling. *J. Common Met.* **1980**, *73*, 273–279. [CrossRef]
5. Joubert, J.M.; Latroche, M.; Percheron-Guégan, A. Hydrogen Absorption Properties of Several Intermetallic Compounds of the ZrNi System. *J. Alloys Compd.* **1995**, *231*, 494–497. [CrossRef]
6. Schlapbach, L.; Riesterer, T. The Activation of FeTi for Hydrogen Absorption. *Appl. Phys. Solids Surf.* **1983**, *32*, 169–182. [CrossRef]
7. Cantor, B.; Chang, I.T.H.; Knight, P.; Vincent, A.J.B. Microstructural Development in Equiatomic Multicomponent Alloys. *Mater. Sci. Eng. A* **2004**, *375–377*, 213–218. [CrossRef]
8. Yeh, J.-W.; Chen, S.-K.; Lin, S.-J.; Gan, J.-Y.; Chin, T.-S.; Shun, T.-T.; Tsau, C.-H.; Chang, S.-Y. Nanostructured High-Entropy Alloys with Multiple Principal Elements: Novel Alloy Design Concepts and Outcomes. *Adv. Eng. Mater.* **2004**, *6*, 299–303. [CrossRef]
9. Marques, F.; Balcerzak, M.; Winkelmann, F.; Zepon, G.; Felderhoff, M. Review and Outlook on High-Entropy Alloys for Hydrogen Storage. *Energy Environ. Sci.* **2021**, *14*, 5191–5227. [CrossRef]
10. Miracle, D.B.; Senkov, O.N. A Critical Review of High Entropy Alloys and Related Concepts. *Acta Mater.* **2017**, *122*, 448–511. [CrossRef]
11. Guo, S.; Ng, C.; Lu, J.; Liu, C.T. Effect of Valence Electron Concentration on Stability of Fcc or Bcc Phase in High Entropy Alloys. *J. Appl. Phys.* **2011**, *109*, 103505. [CrossRef]
12. Yang, X.; Zhang, Y. Prediction of High-Entropy Stabilized Solid-Solution in Multi-Component Alloys. *Mater. Chem. Phys.* **2012**, *132*, 233–238. [CrossRef]
13. Couzinié, J.-P.; Dirras, G. Body-Centered Cubic High-Entropy Alloys: From Processing to Underlying Deformation Mechanisms. *Mater. Charact.* **2019**, *147*, 533–544. [CrossRef]
14. Sahlberg, M.; Karlsson, D.; Zlotea, C.; Jansson, U. Superior Hydrogen Storage in High Entropy Alloys. *Sci. Rep.* **2016**, *6*, 36770. [CrossRef]
15. Akiba, E.; Iba, H. Hydrogen Absorption by Laves Phase Related BCC Solid Solution. *Intermetallics* **1998**, *6*, 461–470. [CrossRef]
16. Akiba, E.; Nakamura, Y. Hydrogenation Properties and Crystal Structures of Ti−Mn-V BCC Solid Solution Alloys. *Met. Mater. Int.* **2001**, *7*, 165–168. [CrossRef]
17. Montero, J.; Zlotea, C.; Ek, G.; Crivello, J.-C.; Laversenne, L.; Sahlberg, M. TiVZrNb Multi-Principal-Element Alloy: Synthesis Optimization, Structural, and Hydrogen Sorption Properties. *Molecules* **2019**, *24*, 2799. [CrossRef]
18. Montero, J.; Ek, G.; Laversenne, L.; Nassif, V.; Zepon, G.; Sahlberg, M.; Zlotea, C. Hydrogen Storage Properties of the Refractory Ti–V–Zr–Nb–Ta Multi-Principal Element Alloy. *J. Alloys Compd.* **2020**, *835*, 155376. [CrossRef]
19. Montero, J.; Ek, G.; Laversenne, L.; Nassif, V.; Sahlberg, M.; Zlotea, C. How 10 At% Al Addition in the Ti-V-Zr-Nb High-Entropy Alloy Changes Hydrogen Sorption Properties. *Mol. Basel Switz.* **2021**, *26*, 2470. [CrossRef]
20. Montero, J.; Ek, G.; Sahlberg, M.; Zlotea, C. Improving the Hydrogen Cycling Properties by Mg Addition in Ti-V-Zr-Nb Refractory High Entropy Alloy. *Scr. Mater.* **2021**, *194*, 113699. [CrossRef]
21. Bouzidi, A.; Laversenne, L.; Zepon, G.; Vaughan, G.; Nassif, V.; Zlotea, C. Hydrogen Sorption Properties of a Novel Refractory Ti-V-Zr-Nb-Mo High Entropy Alloy. *Hydrogen* **2021**, *2*, 399–413. [CrossRef]
22. Strozi, R.B.; Leiva, D.R.; Zepon, G.; Botta, W.J.; Huot, J. Effects of the Chromium Content in (TiVNb)100−xCrx Body-Centered Cubic High Entropy Alloys Designed for Hydrogen Storage Applications. *Energies* **2021**, *14*, 3068. [CrossRef]
23. Park, K.B.; Park, J.-Y.; Kim, Y.D.; Choi, J.-I.; Im, H.-T.; Kang, J.-W.; Kang, H.-S.; Na, T.-W.; Park, H.-K. Study on Hydrogen Absorption and Surface Properties of TiZrVNbCr High Entropy Alloy. *Intermetallics* **2021**, *130*, 107074. [CrossRef]
24. Rodríguez-Carvajal, J. Recent Advances in Magnetic Structure Determination by Neutron Powder Diffraction. *Phys. B Condens. Matter* **1993**, *192*, 55–69. [CrossRef]
25. Gross, K.J.; Carrington, K.R.; Barcelo, S.; Karkamkar, A.; Purewal, J.; Ma, S.; Zhou, H.-C.; Dantzer, P.; Paris-Sud, U.; Ott, K.; et al. Recommended Best Practices for the Characterization of Storage Properties of Hydrogen Storage Materials. 2014. Available online: https://www.energy.gov/eere/fuelcells/downloads/recommended-best-practices-characterization-storage-properties-hydrogen-0 (accessed on 10 May 2022).
26. Aylward, G.; Findlay, T. SI Chemical Data, Third Edition. *J. Chem. Educ.* **1995**, *72*, A109.
27. Couzinié, J.P.; Dirras, G.; Perrière, L.; Chauveau, T.; Leroy, E.; Champion, Y.; Guillot, I. Microstructure of a Near-Equimolar Refractory High-Entropy Alloy. *Mater. Lett.* **2014**, *126*, 285–287. [CrossRef]

28. Abe, J.O.; Popoola, A.P.I.; Ajenifuja, E.; Popoola, O.M. Hydrogen energy, economy and storage: Review and recommendation. *Int. J. Hydrog. Energy* **2019**, *44*, 15072–15086. [CrossRef]
29. Silva, B.H.; Zlotea, C.; Champion, Y.; Botta, W.J.; Zepon, G. Design of TiVNb-(Cr, Ni or Co) Multicomponent Alloys with the Same Valence Electron Concentration for Hydrogen Storage. *J. Alloys Compd.* **2021**, *865*, 158767. [CrossRef]
30. Ek, G.; Nygård, M.M.; Pavan, A.F.; Montero, J.; Henry, P.F.; Sørby, M.H.; Witman, M.; Stavila, V.; Zlotea, C.; Hauback, B.C.; et al. Elucidating the Effects of the Composition on Hydrogen Sorption in TiVZrNbHf-Based High-Entropy Alloys. *Inorg. Chem.* **2021**, *60*, 1124–1132. [CrossRef]
31. Griessen, R.; Strohfeldt, N.; Giessen, H. Thermodynamics of the Hybrid Interaction of Hydrogen with Palladium Nanoparticles. *Nat. Mater.* **2016**, *15*, 311–317. [CrossRef]
32. Burzo, E. (Ed.) *Hydrogen Storage Materials*; Springer: Berlin/Heidelberg, Germany, 2018; ISBN 978-3-662-54259-0.